IEEE Access
Multidisciplinary | Rapid Review | Open Access Journal

Received July 7, 2020, accepted July 25, 2020, date of publication July 29, 2020, date of current version August 10, 2020.

Digital Object Identifier 10.1109/ACCESS.2020.3012714

Integrated Optimization Approach for Aerodynamic, Structural, and Embedded Antenna Design of Joined-Wing SensorCraft

CHENG HE, YUHONG JIA, DONGLI MA, AND GANG CHEN
School of Aeronautic Science and Engineering, Beihang University, Beijing 100191, China
Corresponding author: Cheng He (hecheng93@buaa.edu.cn)

ABSTRACT The joined-wing configuration SensorCraft, presents a more feasible way to meet tough design requirements such as long- endurance and 360-deg radar coverage compared to conventional and flying wing configurations. Proper assessment of the interactions between aerodynamics, structure, and embedded antenna in the optimization of the joined-wing SensorCraft is essential to obtain superior performances. This paper establishes the embedded radar performance estimation model and describes an integrated design process of aerodynamic, structure, and embedded radar performance of such an aircraft. Results show that multi-objective optimization leads to an increase of 14.76% in lift-to-drag ratio, 3.96% and 8.75% in the forward-looking and backward-looking radar detection ranges respectively. Moreover, the structural weight is reduced by 6.0% compared to that of the baseline design. Moreover, sensitivities of the rear wing dihedral angle, endplate height ratio, and joint location of the joined-wing configuration are analyzed in detail.

INDEX TERMS Joined-wing, multi-objective optimization, aerodynamic, structural weight, radar performance.

I. INTRODUCTION

In modern warfare environments, high-altitude long-endurance/surveillance/reconnaissance (ISR) platforms that enable continuous and rapid reaction to dynamic combat operation requirements are playing an increasingly important role, and the SensorCraft is the main representative. According to demonstrations by the Air Force Research Laboratory, SensorCraft is envisioned as a near-space subsonic unmanned aerial vehicle (UAV) with advanced onboard sensor capabilities [1]. Compared with the conventional UAV, SensorCraft need to significantly improve the performance and vision of radar to obtain comprehensive and detailed data. Both the conventional and flying wing configurations are difficult to meet the requirements of long-endurance and 360-deg radar coverage, so the researchers hope to find a more suitable SensorCraft configuration. The joined-wing SensorCraft is one of the most promising research objectives.

Different from the wing-body-tail configuration, the joined-wing configuration uses a sweepback forward wing and a sweepforward rear wing joined in tandem so that it is diamond shaped in both above and front views. The configuration of its forward and rear wings can be used for radar installation to provide omnidirectional field of vision detection, thus allowing fewer potential targets to go undetected. Moreover, the joined-wing SensorCraft also provides the potential to decrease life cycle costs and increase performance [2]. The first joined-wing research was performed by Wolkovitch in 1976 [3]. Since then, this particular configuration has been studied by plenty of researchers trying to capitalize on the structural and aerodynamic advantages.

These studies can be divided into two stages. Early investigations of the joined-wing configuration have decoupled aerodynamics and structures, and reached many useful conclusions. Wolkovitch [4] conducted wind tunnel tests and finite element structural analysis and found that the joined-wing configuration provided several advantages such as low induced drag, light structural weight, and high stiffness. Samuels [5] presented a structural weight comparison between the joined-wing and conventional configurations. The results claimed that the joined-wing weight was 79.4-88% of the conventional configuration weight under aerodynamically equal configurations. Miura *et al.* [6] studied the effects of the sweep angle, dihedral angle, and joint

The associate editor coordinating the review of this manuscript and approving it for publication was Rajesh Kumar.

location on the structural weight of the joined wing using finite element analysis and structural optimization. With respect to aerodynamics, plenty of research has been completed since the first publication of the joined-wing concept. Smith *et al.* [7] conducted a wind tunnel test based on the NASA AD-1 aircraft to measure aerodynamic characteristics using the 12-foot NASA Ames wind tunnel. This research found that the optimum wing joint location was at 60% of the forward wing semi span. Some researchers have performed computational analysis on the joined-wing configuration to understand its aerodynamics better. Oligney *et al.* [8] claimed that joined wing configuration produced lower drag coefficient values than the conventional configuration for lift coefficients above 0.55 using a baseline Houck Joined Wing. Based on wind tunnel testing, Pérez-Álvarez *et al.* [9] analyzed the effects of the rear wing dihedral angle and sweep angle on the aerodynamic characteristics, including cruising efficiency and induced drag coefficient. Later researches paid more attention to the strong coupling effect of this configuration in aerodynamics, structure, and introduced multidisciplinary optimization methods in the design process. Livne [10] claimed that the unconventional configuration made aerodynamics and structure coupled, and the optimal design could not be obtained by considering these aspects in isolation. Schwartz *et al.* [11] analyzed the aero-structural coupling and sensitivity of the joined-wing SensorCraft using Adaptive Modeling Language. Cavallaro and Demasi [12] conducted a detailed review of the previous work on joined-wing configurations and found that multidisciplinary design and optimization are particularly important. Andrews and Perez [13] compared the mission performance of a box-wing and conventional aircraft using a multidisciplinary optimization approach. The results demonstrated the superior performance of the box wing despite fuel volume constraints. These researches indicate that multidisciplinary optimization design plays an important role in obtaining the optimal design process for joined-wing configuration.

The research of the joined-wing configuration on SensorCraft has improved the performance of radar antennas aimed at accomplishing ISR mission requirements, but also increased the complexity of the joined-wing configuration design. The most convenient solution is to integrate airborne early warning (AEW) antennas and apertures into the existing joined-wing platform, while the disadvantages of this method are also obvious. As the arrangement of the AEW antenna is subject to multiple constraints such as installation method, structural strength, volume, and weight, its size and performance are obviously limited to a certain range. Reich *et al.* [14] presented research minimizing antenna deformations using Active Aeroelastic Wing technology. Smallwood *et al.* [15] conducted a study of structurally integrated antennas on a joined-wing aircraft, considering the deflection under typical aerodynamic loads. These researches indicated that the integration into the platform had a negative impact on the performance of the AEW antenna. Therefore, breaking through the subsidiary status of sensors in the design of traditional aircraft and making the performance of sensors a constraint may play a vital role in the overall design. It is necessary to consider the impact of radar antenna installation position and performance evaluation on the airfoil selection, structural weight, and aerodynamic characteristics at the early design phase, that is, to carry out the integrated design of radar-aerodynamic-structure. In the integrated optimization design, the antenna is embedded inside the wing conformally, the structural rigidity is guaranteed by the airframe, and its launch aperture is as large as possible, so as to minimize the negative impact of the aircraft platform on the sensor performance and to improve the overall performance of the joined-wing SensorCraft. However, there is currently no research around the integration of these disciplines in the optimization design.

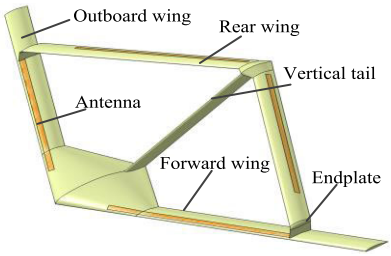

FIGURE 1. Simplified representation of the joined-wing SensorCraft.

This paper proposes the design for the integration of aerodynamics, structure, and embedded radar performance for the joined-wing configuration SensorCraft. The multi-objective optimization uses a combination of aircraft design methods as well as unique structural weight and radar performance models established for this aircraft. Using this method, it is possible to take into account the influence of embedded antenna installation position and performance evaluation on the airfoil selection, structural weight, and aerodynamic characteristics at the early design phase. A comparison of the multi-objective optimization and aerodynamic optimization is presented, which shows that the interdisciplinary interactions, including those that involve the antenna, can influence the optimization results significantly. The influence of specific parameters, unique to the joined-wing configuration, are discussed.

Section II provides the geometric parametrization model and establishes the aerodynamics, structural weight, and radar performance models used in the optimization. Section III presents a description of the optimization problem and the solution process. The case study and results of this optimization problem are then shown in Section IV. Conclusions are given in Section V.

II. GEOMETRIC AND ANALYTICAL MODELS

A. GEOMETRIC PARAMETERIZATION MODEL

The shape of the joined-wing SensorCraft studied in this paper is shown in Fig. 1, which is mainly composed of a forward wing, rear wing, endplate, and vertical tail. Thus, the parameters required for the design of this aircraft are classified into three types: configuration parameters, airfoil design

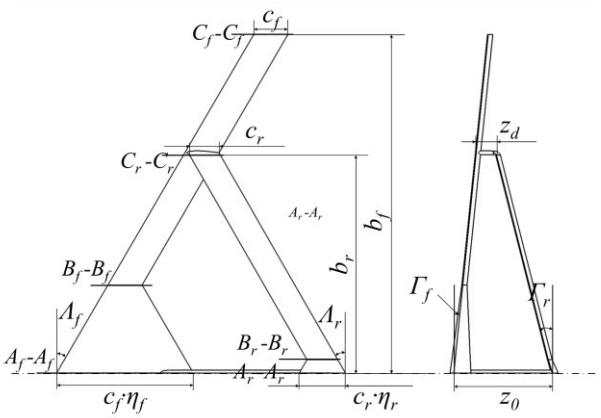

FIGURE 2. Definitions of joined-wing configuration parameters.

parameters, and radar antenna parameters. The parameterized model used is described as follows.

1) CONFIGURATION PARAMETERIZATION

To make the joined-wing configuration parameters more general, dimensionless parameters $\boldsymbol{\psi_D}$ and angle parameters $\boldsymbol{\psi_A}$ are introduced in the parameterization process. The dimensionless parameter $\boldsymbol{\psi_D}$ equals to $\{A_f, b_r/b_f, z_d/z_0, c_r/c_f, \eta_f, \eta_r\}$, where A_f is the forward wing aspect ratio, b_r/b_f the joint location defined as the ratio of wingspan of the forward and rear wings, z_d/z_0 the endplate height ratio defined as the ratio of the endplate height to the vertical tail height, c_r/c_f the chord length ratio, η_f the forward wing root tip ratio, and η_r rear wing root tip ratio. The angle parameters $\boldsymbol{\psi_A}$ equals to $\{\Lambda_f, \Lambda_r, \Gamma_f, \Gamma_r\}$, where Λ_f is the forward wing sweep angle, Λ_r the rear wing sweep angle, Γ_f the forward wing dihedral angle, and Γ_r the rear wing dihedral angle. The main section shape is mainly determined by the airfoils at the wing root, wing tip and the turning position, as shown in Fig. 2.

2) AIRFOIL PARAMETERIZATION

In this section, a new airfoil parameterization method is used in order to adequately describe the shape and provide sufficient control of the design space during the optimization. Based on the class shape transformation (CST) method, a correction function defined by the weighted sum of the non-uniform rational B-spline (NURBS) basis functions is added. By combining these methods, the new approach can overcome the disadvantages of using CST or NURBS independently. The improved parameterization method referred to here as the Class Shape and NURBS Refinement Transformation (CSNT), is described in (1).

$$\begin{aligned} z(\psi) &= (\psi)^{N_1}[1-\psi]^{N_2} \\ &\quad \times \sum_{r=0}^{n} A_r \frac{n!}{r!(n-r)!}\psi^r(1-\psi)^{n-r} + R_k^m(\psi) \\ R_k^m(\psi) &= \sum_{j=0}^{m} p_j \frac{\omega_j N_k^j(\psi)}{\sum_{j=0}^{m} \omega_j N_k^j(\psi)} \end{aligned} \tag{1}$$

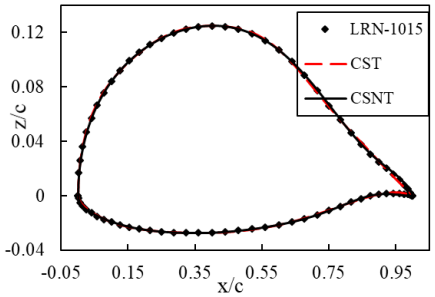

FIGURE 3. Representation of LRN-1015 airfoil by CSNT and CST methods.

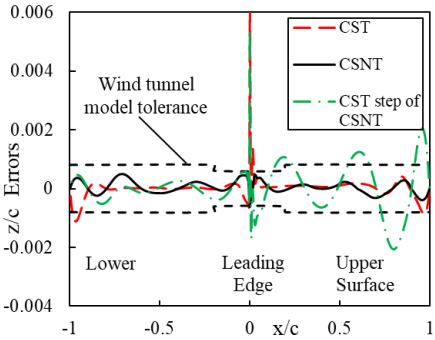

FIGURE 4. Error comparisons of CSNT and CST methods.

Here, the first item is the product of the class function and shape function weighted by the n-order Bernstein polynomial in the CST method [16]. The second item, $R_k^m(\psi)$, is the NURBS correction function with weights $\omega = (\omega_0, \omega_1, \ldots, \omega_m)$. The kth order spline basis function $N_k^j(\psi)$ is computed recursively with a Cox-deBoor recurrence [17].

Fig. 3 presents a comparison of airfoil fitting using the CSNT method and an eighth order CST method with the same number of parameters. The Bernstein Polynomial Order used in the CST method process is 4, and the NURBS correction function uses 4 third-order spline basis functions. Figs. 3 and 4 indicate that the CSNT method enables local shape modification through the use of the NURBS correction function. This is especially useful in the processing of the leading edge, where the CSNT can accurately fit the original airfoil. Although the fitting accuracy of the CSNT method is inferior to the CST method in some positions, there is no significant increase in the residual at the leading edge. This ensures that the fitting accuracy of the entire airfoil is controlled within an acceptable range. In addition, the fitting accuracy of the CSNT method is significantly higher than that of the fourth-order CST method.

3) RADAR ANTENNA PARAMETERIZATION

In this study, to prevent occlusion of the structure, the installation position of the embedded antenna is mainly before the front beam and after the rear beam, as shown in Fig. 5. The parameterization of the embedded radar antenna mainly considers the shape parameters and installation parameters. The shape parameters are mainly the length (L_a) and height (D_a)

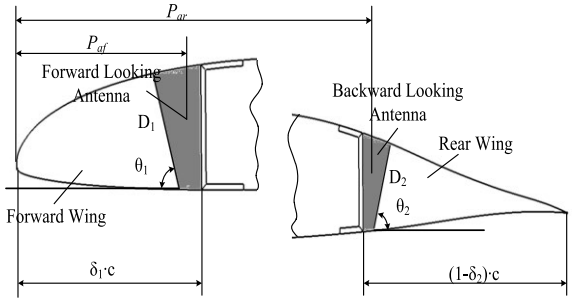

FIGURE 5. Radar antenna installation angle and position.

of the phased array radar antenna surface, and the installation parameters are mainly the installation position (P_{af}, P_{ar}) and angle (θ_1, θ_2) of the forward-looking backward-looking antenna. In addition, there are other parameters, such as, average power, scanning frequency, which are not variables in this article.

B. AERODYNAMIC ANALYSIS MODEL

For high-altitude, high-speed, and low Reynolds number flow problems, laminar flow transition must be considered when performing computational fluid dynamics (CFD) calculations [18]. In this study, the Reynolds averaged Navier-Stokes equations are solved using the γ-Re_θ transition model from Menter and Langtry for closure [19]. This turbulence model is widely used in the numerical calculation of the low Reynolds number flow problems. The numerical simulation in [20], [21] shows that its accuracy and reliability can be guaranteed.

C. STRUCTURE WEIGHT MODEL

Since the joined-wing configuration is a non-planar configuration, the weight estimation model needs to be considered carefully. Based on engineering beam theory [22], a structural weight estimation model suitable for joined-wing configurations has been established. This model builds a connection between the shape parameters varied in the optimization and the structural weight without detailed structural design information. Using force conditions from the aerodynamic model, the weight of the structure designed to withstand bending, shearing, and torsional loads can be calculated. In this section, the structural weight model of the forward wing is established. The model of the rear wing is similar – and therefore not presented here. The total structural weight is obtained using a fitting relationship between the bearing structural weight and the total structural weight. A planform view of the forward wing structural geometry and a representative wing cross-section are shown in Fig. 6.

To unload the wing during flight, the fuel carried is mainly stored in the outer wing and the central fuel tank. If the outer wing is assumed to store fuel in the 60% span position, the volume of the tank outside position, y, is:

$$V(y) = \int_{y}^{0.6L} r_s(y)\cos(\Lambda_s)t(y)dy \tag{2}$$

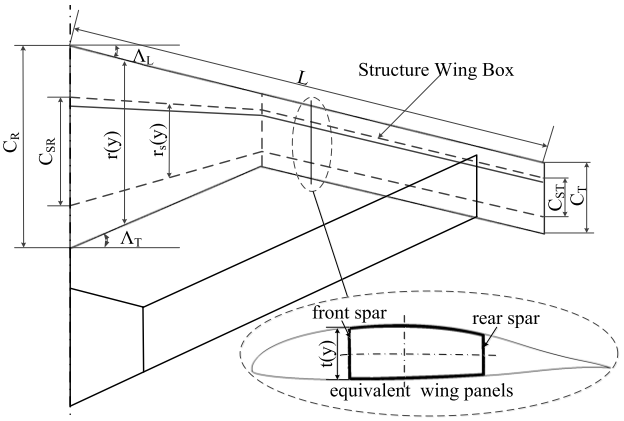

FIGURE 6. The forward wing structure planform geometry and a representative wing-box cross-section.

where Λ_s is the sweep angle of the quarter-chord line, $r_s(y)$ is the structural chord length distribution at the cross-section, and $t(y)$ is the relative structural thickness.

The bending moment $M(y)$ and shear force $F_S(y)$ at position y can be expressed as follows:

$$M(y) = n_s\left[A(y)C_A - \frac{W_{FT}}{W}V(y)C_g + F_{fr}(\frac{b_r}{b_f}L - y)\right] \tag{3}$$

$$F_S(y) = n_s\left[A(y) - \frac{V(y)}{2V(0)}W_{FT} + F_{fr}\right] \tag{4}$$

where $A(y)$ is the combination of aerodynamic forces outside the y position, C_A is the aerodynamic center given by the aerodynamic model, C_g is the center of gravity of the fuel, F_{fr} is the force of the endplate between the forward and rear wings, and n_s is the overload coefficient.

Using the bearing structural weight theory, the forward wing primary structural weight can be obtained by:

$$W_{fprim} = 2k_1\int_0^L [\rho_m r_s(y)\cos\Lambda_s t(y)\varepsilon(\frac{M(y)}{r_s(y)\cos\Lambda_s t^2(y)E})^e + \frac{\rho_m F_S(y)}{\sigma_s} + \frac{\rho_m M(y)\sin\Lambda_s(t(y)+r_s(y))}{\sigma_s t(y)r_s(y)}]dy \tag{5}$$

where the three weights in the integral are the bending, shear, and torsional material weight per unit length, respectively. Additionally, the variable ρ_m is the material density, σ_s is the allowable shear stress, E is the elastic modulus, ε is the instability factor, e is the instability index, and k_1 is the weight fitting factor [22].

For high aspect ratio aircraft, the aeroelastic effects should be considered even in the early weight estimations. However, the detailed aeroelastic effects on weight can be obtained only in case a detailed knowledge exists of the spanwise torsional stiffness variation and such details as the position of the inertia and flexural axis. For simplicity, the torsional stiffness in this model is increased by resizing the corresponding equivalent wing panels so that the divergence and reversal speeds are greater than the critical speed. Resizing the panels to increase the torsional rigidity directly affects its structural weight.

An empirical weight change will have the following appearance:

$$W_{fa} = fa\frac{\rho_m}{G}q_D\frac{(b\cos\Lambda_L)^3(1-\sin\Lambda_{1/2})}{(t/c)_{ref}^2(1-M_D\cos^2\Lambda_{1/2})^{1/2}} \quad (6)$$

where q_D and M_D denote the dynamic pressure and the Mach number at the design diving speed, respectively. The ratio $(t/c)_{ref}$ refers to wing station at 70% semi-span outboard from the root, f_a is aeroelastic fitting factor [22].

Although the beam section model considers the materials required to resist the primary forces caused by aerodynamic loads, it did not consider the secondary weight W_{sec} such as the weight of the wing ribs W_{rib} and the weight of the high-lift devices at the leading and trailing edges (W_{fle} and W_{fte}), as well as the material required to resist additional aerodynamic loads W_{con}. The primary purpose of the wing ribs is to resist torsional loads on the wing as well as to strengthen the wing skin to prevent buckling and transfer the loads from the high-lift devices and propulsion systems to the wing-box structure. Instead of directly modeling these effects, they are explained based on the empirical relationship given by Torenbeek [22].

As all component weights are based on non-configuration specific inputs and relationships, it can be extended to unconventional wing designs. More details about these components weight models and the assumptions used in derivation are presented in Torenbeek wing weight model [22].

$$W_{f\,\mathrm{sec}} = W_{rib} + W_{fle} + W_{fte} + W_{con} \quad (7)$$

In summary, the forward wing structural weight can be obtained by:

$$W_{fstr} = W_{fprim} + W_{fa} + W_{f\,\mathrm{sec}} \quad (8)$$

D. RADAR PERFORMANCE MODEL

The joined-wing SensorCraft has specific performance requirements, including radar detection ranges R_f and R_r, and a radar height coverage H_{radar} on the safety line R_{safe}. In order to reduce interference due to ground clutter and improve the ability of the system to detect targets from moving clutter, the pulse-Doppler (PD) radar system is selected in this paper. Additionally, this radar is the most suitable for installation in aircraft wings because of the extremely small thickness of the slot antennae. Significant research on the calculation of radar performance has been carried out since Omberg and Norton presenting the radar distance equation [23]. Over time, the required parameter accuracy has been continuously improved. With the development of statistical signal theory, Marcum [24] proposed that the detection probability was related to the signal-to-noise ratio in the radar distance equation. Using the Swerling radar target fluctuation model, Blake considered system noise and atmospheric losses to define a radar equation more suitable for modern radar systems with more complex features and modes and offered high precision results [25]. The effects of target fluctuation models, system parameters, and environmental factors have subsequently been studied.

1) DETECTION RANGE

As shown in Fig. 5, the antennas are embedded in the forward and rear wings. The antenna height, aperture, and gain are influenced by the chord length, airfoil thickness, and antenna installation angle. The antenna length affects the beamwidth, which impacts the Doppler bandwidth and the minimum signal-to-noise ratio. Therefore, the radar detection range model can be established using the wing shape parameters and the antenna installation angle.

The phased-array AEW radar beamwidth varies with scanning angle in the azimuthal plane. To achieve a roughly equal detection distance in each direction, increasing the dwell time and compensating for signal-to-noise ratio losses is necessary [26]. The beam center pointing angle, θ_n, is given by:

$$\theta_n - \theta_{n-1} = \frac{1}{2}(1-\rho_0)(\theta_{B,n} + \theta_{B,n-1}) \quad (9)$$

where $\theta_{B,0}$ is the normal beamwidth calculated using $\theta_{B,0} = 50.8\ \lambda/(N_1 d_1)$. Here, N_1 is the number of array elements, d_1 is array element spacing and is generally equal to half of the wavelength. $\theta_{B,n}$ is the beamwidth of the nth beam position obtained by $\theta_{B,n} = \theta_{B,0}/cos\theta_n$. ρ_0 is the overlapping coefficient of the adjacent scanning beam. In this paper, when $\rho_0 = 0$, this indicates that adjacent beams are non-overlapping.

To ensure the same detection distance on all sides of the radar, the accumulation time of the beam position pulse should increase. The accumulation time can be obtained by $t_n = t_0/cos^2\theta_n$, where t_0 is normal pulse accumulation time. Pulse fill time can be calculated from $t_f = 2R_{max}/c_1$. Thus, the total search time for $0°-60°$ is

$$t_s = \sum_{n=1}\frac{\theta_n}{\theta_{B,n-1}}(t_n + t_f) \quad (10)$$

For PD radar systems, Doppler bandwidth and the normal pulse accumulation time is associated with $B_n = 1/t_0$.

When the AEW radar detects the target, many types of PRF are often adopted to eliminate the blurring of range and speed measurements [27]. For example, when the m/n criterion is applied, the single scan detection probability is expressed as follows:

$$P_D = \sum_{i=m}^{n} C_n^i P_d^i (1-P_d)^{n-i} \quad (11)$$

where P_d is the single-frame detection probability. In this paper, the *2/4* detection criterion is adopted. The false alarm probability of the detection unit P_{fa} is then

$$P_{fa} = \frac{1}{N_f}\left(\frac{0.693T_d}{C_n^m N_g T_{fa}}\right)^{\frac{1}{m}} \quad (12)$$

here, T_d is a multiple of the PRF total dwell time which can be obtained by $T_d = nt_0$. N_f is the number of Doppler filters calculated by $N_f = 4v_{max}/(\lambda B_n)$, where v_{max} is the target maximum radial speed of 1000m/s. N_g is equal to

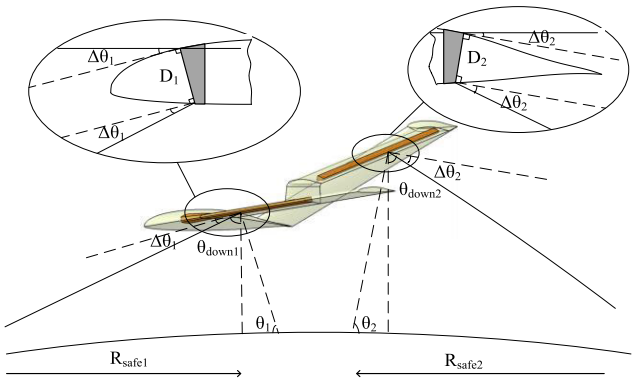

FIGURE 7. Installation angle and height coverage of the radar antennas.

14000 and is the number of range gates in the unambiguous output distance interval. T_{fa} is the average warning time and is equal to 1s.

For the Swerling I target model [25], the single-frame detection probability, and the minimum signal to noise ratio are associated with the following equation:

$$(S/N)_{\min} = \frac{\ln P_{fa}}{\ln P_d} - 1 \tag{13}$$

Finally, using (9) - (13), the detection range can be calculated by:

$$R_{\max} = \left[\frac{P_{av} G_T G_R \lambda^2 \sigma}{(4\pi)^3 L_g k T_0 B_n (S/N)_{\min}} \right]^{\frac{1}{4}} \tag{14}$$

where P_{av} is the average power. G_T and G_R are the transmitter and receiver gain, respectively. σ is the target radar cross-section (RCS); λ is the working wavelength. L_g is the system loss. k is the Boltzmann constant. T_0 is the equivalent noise temperature. The antenna gain can be obtained using $G = 4\pi\rho_1 L_a D_a/\lambda^2$, where L_a is the length of the antenna, D_a is the height, and ρ_1 is the aperture efficiency of the antenna [25].

2) HEIGHT COVERAGE

In order to ensure the security of the SensorCraft, it is essential to maintain continuous monitoring on the safety line, R_{safe}. Fig. 7 shows the installation angle and height coverage of the embedded radar antennas.

According to the geometric relationship in Fig. 7, (15) is obtained.

$$\left.\begin{aligned} \theta_1 &= \Delta\theta_1 + \theta_{down1} - \alpha \\ \theta_2 &= \Delta\theta_2 + \theta_{down2} + \alpha \end{aligned}\right\} \tag{15}$$

where θ_1 and θ_2 are the antenna installation angles; α is the angle of attack; $\Delta\theta$ is the radar scan yaw angle; θ_{down1} and θ_{down2} are the lower viewing angles of the safety distance coverage area.

When the antenna scans in the pitch plane, the gain of the antenna is a maximum, which can be approximated by a Gaussian function expressed as follows:

$$G(\Delta\theta) = \exp(-2.78\Delta\theta^2 / \varphi_{B,0}^2) \tag{16}$$

TABLE 1. Comparisons of published data and calculated data.

Target RCS /(m^2)	5	1	0.1
Published data /(km)	300	200	100
Performance model/(km)	295.1	197.1	108.4
Error /(%)	1.63	1.45	8.4

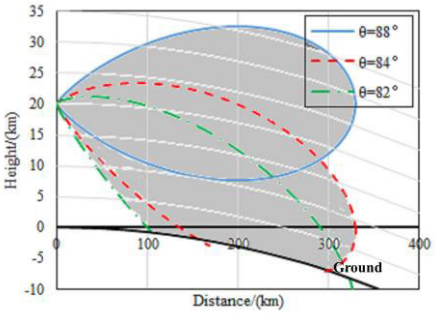

FIGURE 8. Height coverage at different radar installation angles, the angle of attack 2°.

where $\varphi_{B,0}$ is the normal beamwidth in the pitch plane obtained by $\varphi_{B,0} = 50.8\lambda/(N_2 d_1)$ where N_2 is the number of wide side array elements. Assuming that low-altitude detection distance equals R_{safe}, $\Delta\theta$ can be obtained using:

$$R_{safe}^4 = \frac{P_{av}(\Delta\theta) G_T(\Delta\theta) G_R(\Delta\theta) \lambda^2 \sigma}{(4\pi)^3 L_{g1} k T_0 B_n (S/N)_{\min}} \tag{17}$$

where L_{g1} is the sum of the equipment loss. The double-range distance loss at the safety distance, R_{safe}, is generally equal to 100km. Using these relationships, the antenna size and installation angle can be obtained in order to satisfy the required detection range and height coverage.

The height coverage and the safety distance are related by the following equation:

$$H_{radar} = R_{safe} / \tan(\theta - \Delta\theta) \tag{18}$$

The radar performance model was verified using a PS-890 AEW radar system. The radar system parameters are as follows: the radar aperture size was 8m ×0.6m, the number of antenna vibrators of each array was 178 × 12, the array power was 3kW, and the common frequency was 2.54GHZ [26]. For this system, the double-range atmospheric loss at 400km is approximately 3.8dB, and the noise figure of the receiver equals to 2.3dB. Table 1 shows the verification results. Compared with the published data for the system, the calculation error is acceptable. Therefore, the accuracy of the performance model the present radar model is acceptable for the present optimizations.

Analysis of installation angle and frequency show that when the antenna installation angle is 88°, for the angle of attack in consideration, the antenna array plane is perpendicular to the ground, and the ground cannot be covered. When the radar installation angle is reduced, the radar can achieve the coverage of 100km on the ground (As shown in Fig. 8). Fig. 9 shows that the radar detection distance increases first and then decreases with the variation of frequency. The increase

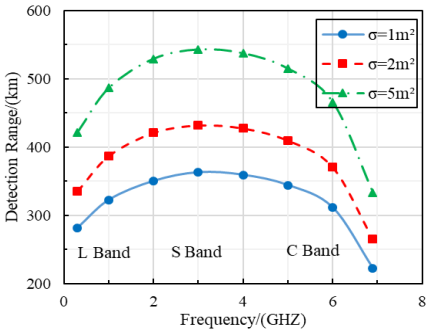

FIGURE 9. The relationship between wavelength and detection range.

TABLE 2. Aircraft design condition.

Design condition	Value	Design condition	Value
Total weight W_{to}/(kg)	28000	Cruising speed V/(Ma)	0.65
Wing area S/(m^2)	290	Angle of attack α/(°)	2
Cruising altitude H/(km)	20	-	-

of antenna gain leads to an increase in detection range at low frequencies such as L-band. However, as the frequency increases, the beamwidth of the azimuthal wave becomes narrow, the dwell time and the coherent accumulation time are shortened, and the atmospheric loss becomes large. These changes offset the increase due to the antenna gain, and the detection distance ultimately decreases.

III. OPTIMIZATION PROBLEM

As shown in Fig. 1, a joined-wing configuration SensorCraft is mainly composed of a forward wing, rear wing, endplate, and vertical tail. The design requirements of the aircraft are listed in Table 2. The shape of the forward wing is in a flying wing form. To ensure 360° radar coverage in the azimuthal plane, four radar antennas are installed in the forward and rear wings. The wing leading edges are parallel to the wing trailing edges from the vertical view to meet certain stealth requirements. The forward-looking and the backward-looking antennas are located ahead of the 0.3c position and after the 0.65c position, respectively (Fig. 5). The AEW antenna parameters are as follows: the long side length is 18m, the average power of each array is 9kW, the conventional frequency is 3.2GHz, and the target RCS is 1m^2.

This optimization aims to find a joined-wing SensorCraft configuration to achieve long-endurance flight and large area radar coverage while meeting all the constraints. The previous section described the aerodynamic, structural and radar performance analysis models needed to determine the performance of the joined-wing SensorCraft. These analysis models are not independent, each depends on the results of one or more disciplinary analysis model. The interdisciplinary couplings and flow of information are presented in Fig. 10.

A. OBJECTIVE

To achieve the overall performance requirements of joined-wing SensorCraft, the optimization objectives of various disciplines are mainly the following three aspects.

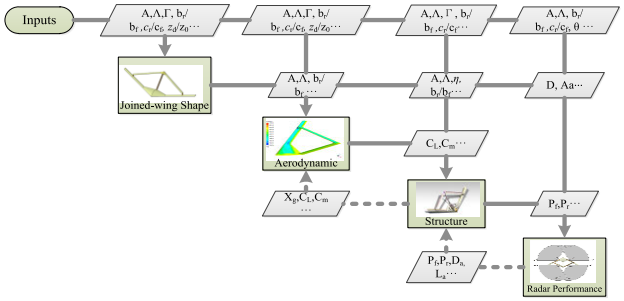

FIGURE 10. Flow of information in the multidisciplinary optimization.

TABLE 3. Range of design variables.

Parameter	Range
Forward wing aspect ratio A_f	19-27
Forward wing sweep angle Λ_f(°)	30-45
Forward wing dihedral angle Γ_f(°)	4-10
Rear wing dihedral angle Γ_r(°)	10-25
Joint location b_r/b_f	0.65-0.95
Endplate height ratio z_d/z_0	0.1-0.4
Chord length ratio c_r/c_f	0.8-1
Forward wing root tip ratio η_f	3-5
Rear wing root tip ratio η_r	1.5-2.5
Antenna installation angle θ(°)	70-90

With respect to aerodynamics, the cruise lift-to-drag ratio (K), is required to be as large as possible. When the total take-off weight is unchanged, the lighter the structural weight W_{str} means the heavier the fuel or other equipment, which means improved performance. The structural weight (W_{str}) is required to be small. For embedded radar performance, the radar detection range for targets with $RCS = 1\text{m}^2$ at cruising altitude (R_f, R_r), is to be maximized. The optimal result of the multi-objective optimization is obtained by evaluating the equilibrium solutions in the Pareto optimal front.

B. VARIABLES

The design variables can be divided into three categories: airfoil parameterization variables $\boldsymbol{x}$ described in Section II, configuration parameters including angles $\boldsymbol{\psi_A}$ and dimensionless $\boldsymbol{\psi_D}$ variables, and antenna installation variables $\boldsymbol{\theta}$ (as shown in Table 3). The dimensionless parameter $\boldsymbol{\psi_D}$ equals to $\{A_f, b_r/b_f, z_d/z_0, c_r/c_f, \eta_f, \eta_r\}$, where A_f is the forward wing aspect ratio, b_r/b_f the joint location defined as the ratio of wingspan of the forward and rear wings, z_d/z_0 the endplate height ratio defined as the ratio of the endplate height to the vertical tail height, c_r/c_f the chord length ratio, η_f the forward wing root tip ratio, and η_r rear wing root tip ratio. The angle parameters $\boldsymbol{\psi_A}$ equals to $\{\Lambda_f, \Lambda_r, \Gamma_f, \Gamma_r\}$, where Λ_f is the forward wing sweep angle, Λ_r the rear wing sweep angle, Γ_f the forward wing dihedral angle, and Γ_r the rear wing dihedral angle. The antenna installation variable $\boldsymbol{\theta}$ equals to $\{\theta_1, \theta_2\}$ where θ_1 is the forward-looking antenna installation angle, θ_2 the backward-looking antenna installation angle. The ranges for these variables are expected to be as wide as possible while remaining within the domain where

TABLE 4. Constraints of optimization problem.

Aerodynamic constraints		radar height coverage constraints	
Cruise lift	$C_L=C_W$, $\lvert\Delta C_L/C_L\rvert\le 5\%$	height coverage	$H_{radar}\ge H$
		radar installation constraints	
Pitching moment	$C_m=0$	The forward-looking antenna position	$P_{af}\le\delta_1 c$
Static stability	$-C_{m\alpha}/C_{L\alpha}\ge 10\%$	The backward-looking antenna position	$P_{ar}\ge\delta_2 c$

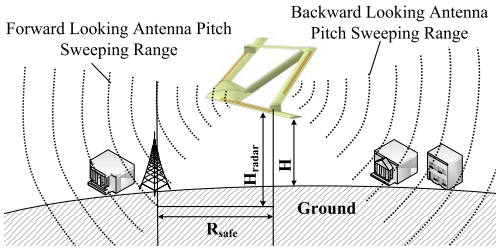

FIGURE 11. Schematic diagram of radar height coverage.

the present multidisciplinary analysis is still effective. For some variables, the ranges are chosen based on references in the literature and geometric requirements. For other variables, large bounds which will never be approached are selected.

C. CONSTRAINTS

As shown in Table 4, there are three primary groups of constraints: aerodynamic, radar height coverage and installation position. The aerodynamic constraints are needed to ensure the joined-wing SensorCraft cruise steadily. Here, the center position of the aircraft is estimated based on the forward and rear wing area roughly. In addition to the radar height coverage constraints shown in Fig. 11, the radar coverage height (H_{radar}) is required to be greater than the aircraft cruise altitude (H) to achieve high and low altitude coverage on the safety line R_{safe} and ensure the security of the joined-wing SensorCraft itself. The installation constraints mainly consider the interference of radar antenna installation and wing structure. The forward-looking antenna (P_{af}) must be installed before the forward wing front beam position $\delta_1 c$, and the backward-looking antennas (P_{ar}) must be installed behind the rear wing back beam position $\delta_2 c$.

A constrained multi-object optimization problem can be described as (19)

$$\begin{cases} Max \;\; K,\; R \\ Min \;\; W_{str} \\ \text{d.v.} x = (\boldsymbol{\psi_D}, \boldsymbol{\psi_A}, \boldsymbol{x}, \boldsymbol{\theta}) \\ st. \quad |\Delta C_L / C_L| \le 5\%,\; C_m = 0,\; -C_{m\alpha}/C_{L\alpha} \ge 10\% \\ \qquad H_{radar} \ge H,\; P_{af} \le \delta_1 c,\; P_{ar} \ge \delta_2 c \end{cases} \tag{19}$$

D. OPTIMIZATION PROCESS

The optimization process is shown in Fig. 12, the aircraft is first designed and parameterized according to the specified performance requirements, and initial sample points are taken

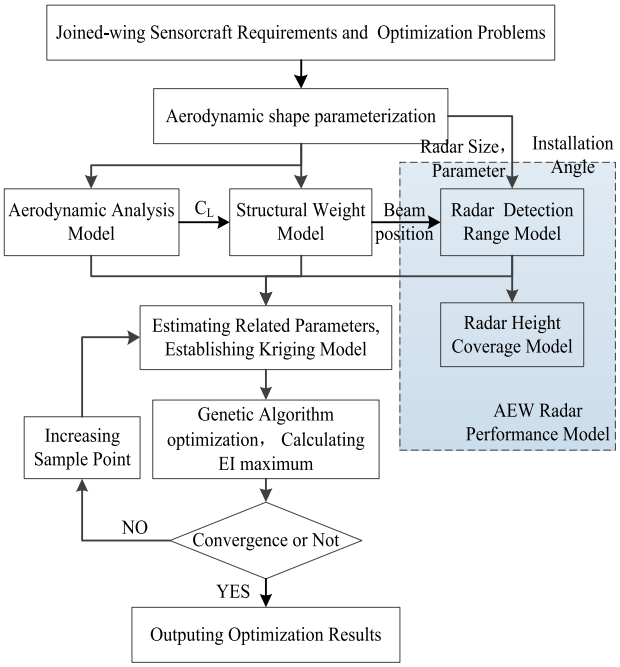

FIGURE 12. Optimization design flowchart.

using Latin Hypercube Sampling first [28]. Next, aerodynamic, structural, and radar performance are computed, and the initial Kriging surrogate models are established [29]. Then, the NSGA-II is selected for optimization. Adaptive sampling is performed based on the maximum value of the expected improvement (EI) function given in (20) [30]. Finally, the process checks if the convergence criterion is met. If not, the current optimal design is added to the next modeling optimization sample – and the process is repeated until convergence. In the present approach, a criterion is applied to select additional sample points during the iterative optimization process. This method improves the accuracy of the response surface and the global optimum efficiency, thereby reducing the dependence on the initial sample set.

$$E[I(x)] = \begin{cases} (y_{\min}-\hat{y})\Phi\left(\frac{y_{\min}-\hat{y}}{s}\right)+s\varphi\left(\frac{y_{\min}-\hat{y}}{s}\right), & s>0 \\ 0, & s=0 \end{cases} \tag{20}$$

where y_{min} is the minimum adaptation value in the design space. Φ, φ, $\hat{y}$, and s are the standard distribution, the normal density, the predicted value, and the prediction standard deviation, respectively. It can be seen from the EI function: when the predicted value of the agent model is less than the current minimum fitness value, the first item will become relatively large. The focus of the search is near the current minimum fitness value, which strengthens the local search ability of the agent model; When the predicted value is close to the current minimum fitness value, that is, the overall prediction accuracy of the model is low, the second item value is relatively large. At this time, the proxy model focuses the search on areas with poor prediction accuracy, which can strengthen the Kriging model global search capability.

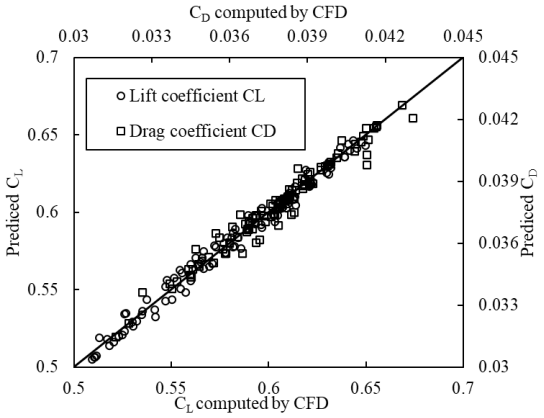

FIGURE 13. Comparisons of predicted values by Kriging model and CFD calculated values.

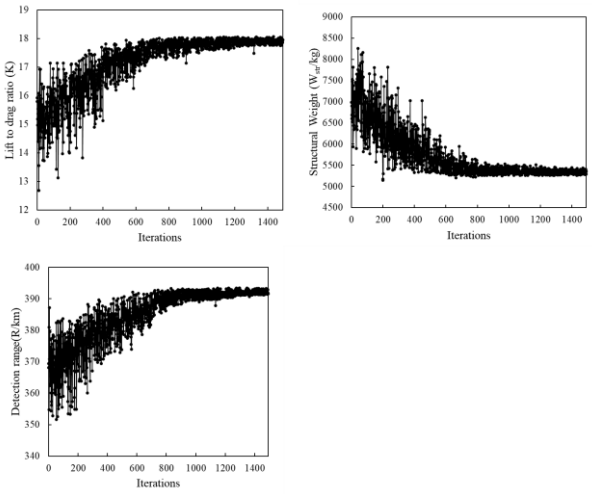

FIGURE 14. The convergence of the multidisciplinary optimization.

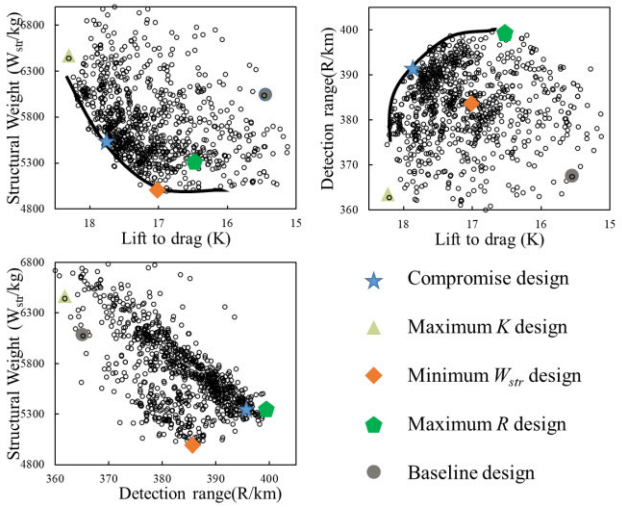

FIGURE 15. Results and Pareto fronts of the multi-objective genetic algorithm optimization.

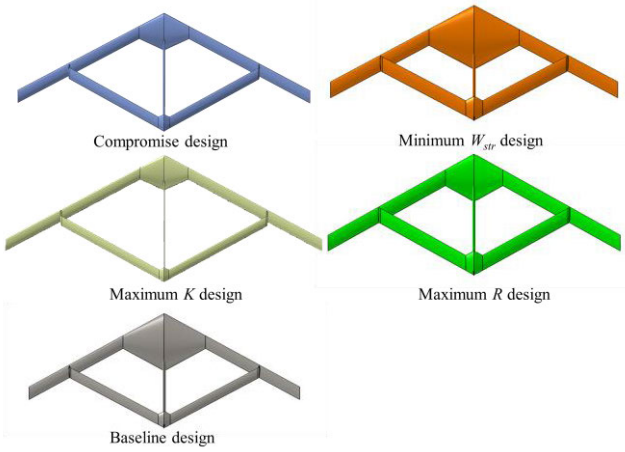

FIGURE 16. Aircraft shapes before and after optimization.

IV. RESULTS AND ANALYSIS

A. RESULTS

In the process of the optimization design, the high fidelity CFD analysis solver is time-consuming. Initial Kriging models for the optimization objectives and constraints of aerodynamics using 450 sample points is established, and then the maximum value of the EI function is used to add 150 sample points to further improve the accuracy. Fig.13 shows comparison of the calculated values of CFD with the predicted values of Kriging model.

The final Kriging models that meet the accuracy requirements are used for multidisciplinary optimization calculation. In terms of optimization time, if the high fidelity CFD analysis solver is used, it takes about 240 hours. When the Kriging models are used, it takes only 96 hours. The time required for multidisciplinary optimization reduced significantly. Fig. 14 shows the convergence history of the multidisciplinary optimization process.

Fig. 15 provides the Pareto optimal front for maximizing the lift-to-drag ratio, K, and minimizing both of structural weight, W_{str}, and the average of the forward and backward detection range, R. The designs on the Pareto front provide the designers with alternatives to trade the relative advantages of each objective: one may choose a high lift-to-drag ratio but a relatively heavy structural weight and a low radar detection range or a compromise proposal. As shown in Fig. 15, the shape of the Pareto front of this optimization is unique: it is initially very steep, then its slope seems to decrease. Therefore, it is worth sacrificing a little lift-to-drag ratio to attain a light structure and a high radar detection range (the compromise design is represented by the star shape).

The shapes and the optimization results are the baseline, maximum K, minimum W_{str}, maximum R, and compromise design are presented in Fig. 16 and Table 5. Compared with the baseline design, the compromise design of the multi-objective optimization shows a significant improvement in aerodynamic, structure and radar performance. The lift-to-drag ratio of the multi-objective compromise result is 14.76% higher than the baseline design. Moreover, the structural weight is reduced by 6.0%, and the forward-looking and

TABLE 5. Overall aircraft optimization results.

	Parameter	Baseline	Maximum K	Minimum W_{str}	Maximum R	Compromise
design variables	Λ_f/(°)	30	30.03	30	31.83	30.19
	Γ_f/(°)	5	7.27	7.95	9	7.04
	Γ_r/(°)	10	14.1	15.69	12.1	15.28
	b_r/b_f	0.7	0.66	0.65	0.65	0.65
	η_f	4.5	3	4	3	3.1
	η_r	1.6	1.82	1.5	1.54	1.5
	c_r/c_f	0.8	0.81	0.94	0.95	0.93
	A_f	20	26.9	19	19.2	23.04
	z_d/z_0	0.2	0.28	0.15	0.16	0.19
objectives	W_{str}/(kg)	5962.3	6374.5	4987.2	5390.1	5605.9
	R_f/(km)	381.4	377.6	391	403.4	396.5
	R_r/(km)	354.3	345.1	380.9	395.7	385.3
	Predicted K	15.51	18.23	17.02	16.71	17.8
	Real K	15.49	18.17	17.13	16.67	17.85
constraints	*Predicted* $\lvert\Delta C_L/C_L\rvert$	0.15%	4.84%	3.9%	2.66%	0.78%
	Real $\lvert\Delta C_L/C_L\rvert$	0.13%	4.56%	3.78%	2.57%	0.86%
	Predicted C_m	0.002	0.004	0.003	0.002	0.002
	Real C_m	0.002	0.002	0.002	0.004	0.002
	Predicted $-C_{m\alpha}/C_{L\alpha}$	0.143	0.103	0.154	0.152	0.124
	Real $-C_{m\alpha}/C_{L\alpha}$	0.147	0.113	0.163	0.147	0.121
	P_{af}	0.3	0.3	0.3	0.3	0.3
	P_{ar}	0.65	0.65	0.65	0.65	0.65
	H_{radar}/km	20.42	20.12	20.53	22.34	20.91

backward-looking radar detection ranges increase by 3.96% and 8.75%, respectively.

From the detailed design parameters of maximum lift-to-drag ratio design, it is observed that the aspect ratio is close to the upper boundary, and the joint location and the root tip ratio are near the lower boundaries. Compared to the maximum lift-to-drag ratio design, the compromise design has a significant reduction of the optimized forward wing aspect ratio, a slight decrease of the forward wing dihedral angle, and an obvious increase of the chord length ratio. The structural weight of the multi-objective compromise design is reduced by 12.06% compared with that of maximum lift-to-drag ratio design, and the forward-looking and backward-looking radar detection ranges increase by 5.01% and 11.65%, respectively. However, the lift-to-drag ratio shows a 2.36% reduction.

The detailed design parameters of minimum structural weight design show that the aspect ratio, the endplate height ratio, and the joint location are close to the lower boundaries. Compared to the minimum structural weight design, the lift-to-drag ratio, the forward-looking and backward-looking radar detection ranges of the compromise design shows an increase of 4.58%,1.41% and1.16%, respectively. However, the structural weight is increased by 12.4%.

From the detailed design parameters of maximum radar detection range design, it is observed that the aspect ratio, the joint location and the root tip ratio are near the lower boundaries, and the chord length ratio is close to the upper boundary. The lift-to-drag ratio of the multi-objective compromise design is increased by 6.52% compared with that of maximum radar detection range design. However, the structural weight is increased by 4%, and the forward-looking and backward-looking radar detection ranges decrease by 1.71% and 2.63%, respectively.

TABLE 6. The performance of the section shapes at the turning position before and after optimization.

	Parameter	Baseline	Optimized Forward	Optimized Rear
variables	θ_1/(°)	77	76.2	-
	θ_2/(°)	83.8	-	76.2
objectives	*Predicted* K_1	38.88	62.84	63.94
	Real K_1	38.54	61.47	63.21
	R_f/(km)	383.8	401.4	-
	R_r/(km)	357.2	-	391.8
constraints	*Predicted* C_l	0.906	1.018	0.876
	Real C_l	0.902	1.004	0.881
	H_{radar}/(km)	20.42	20.91	20.94

The section shapes at the turning position of the forward and rear wings (B_f-B_f, B_r-B_r, as shown in Fig. 2) have been chosen as the representative of the section shape of the joined-wing SensorCraft. The optimization results of the section shapes at the turning position are listed in Table 6. Compared with the baseline design section shape, the lift-to-drag ratio and the detection range of the optimized section shape at the forward wing turning position are increased by 61.6% and 4.6%, respectively. The optimized section shape at the rear wing turning position shows an increase of 64.5% and 9.7% for lift-to-drag ratio and detection range, respectively.

Fig. 17 shows the section shapes at the turning position and antenna installation positions before and after optimization.

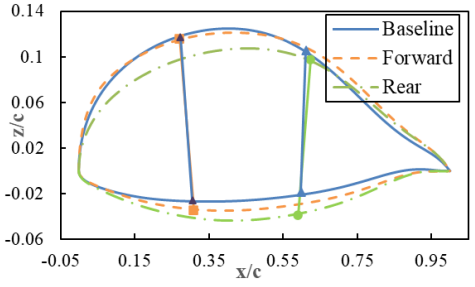

FIGURE 17. Comparisons of the sectional shapes at the turning position and antenna installation positions before and after optimization.

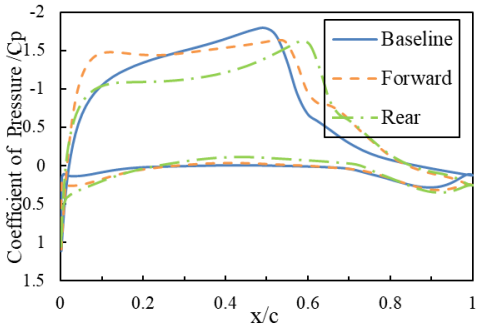

FIGURE 18. Comparisons of pressure distributions before and after optimization.

Compared to the baseline section shape, the optimized forward section shape has an obviously increased thickness and a reductions camber and leading edge radius. Similarly, the maximum thickness of the optimized rear section shape is increased, and the maximum thickness position is moved towards the trailing edge. The lower surface moves downward due to the installation of the antenna, reducing the loading of the middle of the section shape. As a consequence, the lift coefficient is decreased. However, this reduction is limited, and the overall aerodynamic characteristics are significantly improved.

Fig. 18 presents a comparison of the resulting pressure distributions. The results show that the optimized forward section shape creates faster leading-edge flow than the baseline section shape, and the pressure gradient of the upper surface becomes less adverse. The middle of the optimized rear section shape upper surface is flat, which contributes to moving the negative pressure gradient region towards the trailing edge. For the optimized section shapes, a large zone of laminar flow area remains, and trailing edge separation is weakened. This is likely caused by the downstream movement of the shock wave position and the significant weakening of the shock wave strength. As a result, the lift-to-drag ratio has increased significantly.

B. SENSITIVITY ANALYSIS

In this section, the sensitivity coefficients of the objectives for the joined-wing configuration parameters are calculated. As observed in Figs. 19 and 20, there is a strong correlation

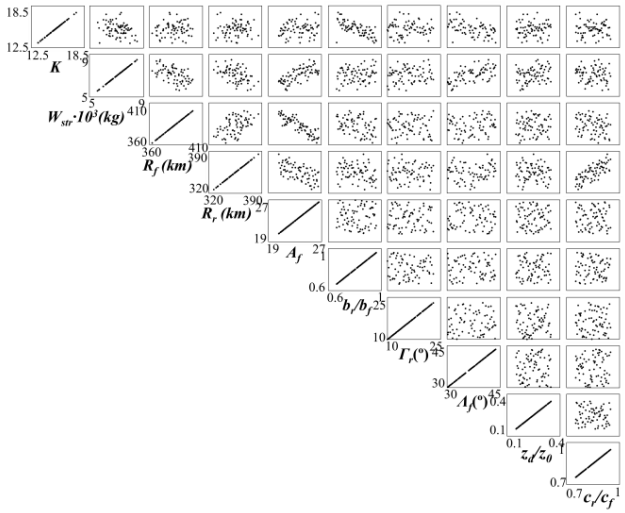

FIGURE 19. Relationship between objective parameters and design variables.

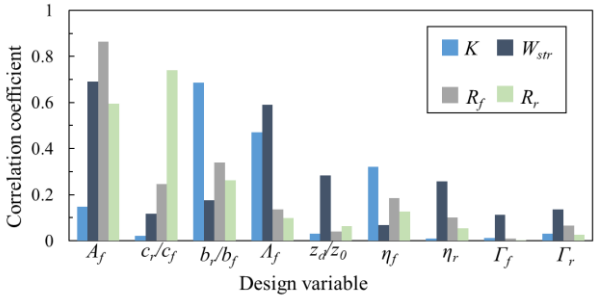

FIGURE 20. Correlation coefficients between design variables and objectives.

between the structural weight and the forward wing aspect ratio, sweep angle, and endplate height ratio. This is because these parameters directly affect the wing length, which causes the loaded bending moments to change drastically. The parameters that impact the radar detection range most significantly are the forward wing aspect ratio, wing root tip ratio, joint location, and the chord length ratio. These parameters directly affect the chord length of the forward and rear wings, which changes the antenna aperture. Additionally, the joint location, sweep angle, forward wing root tip ratio, and aspect ratio have a significant influence on the aerodynamic characteristics of the aircraft. These parameters can implicitly change the forward and rear wing aspect ratio, or result in mutual interference between the forward and rear wing flow fields, thereby affecting aerodynamic characteristics. Because some of the parameters of the joined-wing configuration are unique compared to the conventional configuration, some parameters are analyzed in detail here.

1) THE REAR WING DIHEDRAL ANGLE

As shown in Fig. 21, the aerodynamic coefficients, structural weights, and detection ranges vary slightly with the rear wing dihedral angle, Γ_r. The aerodynamic results indicate that the

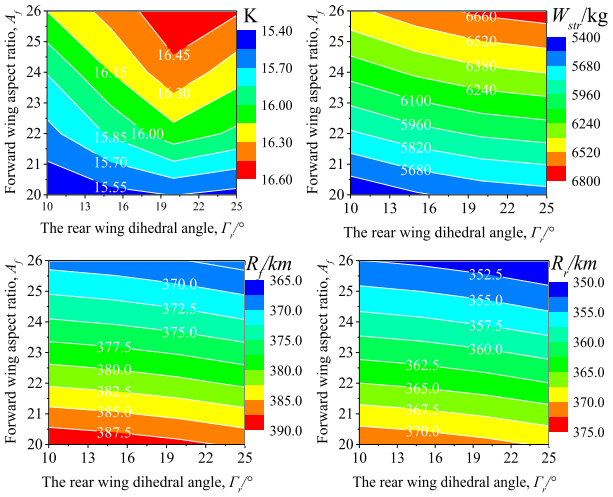

FIGURE 21. Aerodynamic characteristics, structural weights, and detection ranges vary with the rear wing dihedral angle.

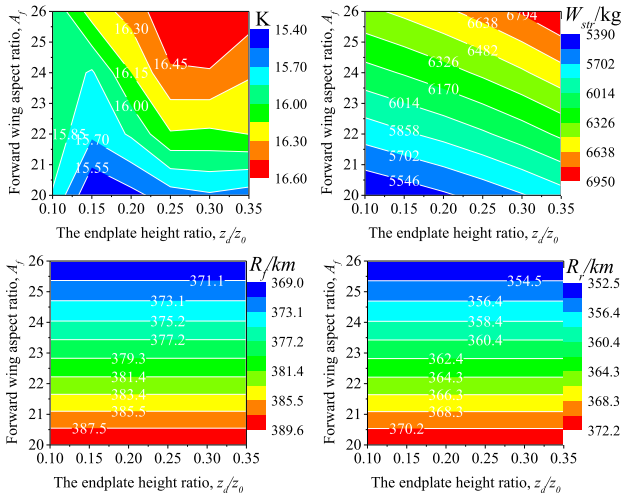

FIGURE 22. Aerodynamic characteristics, structural weights, and detection ranges vary with the endplate height ratio.

forward wing wash strongly impacts the rear wing for small rear wing dihedral angles, and the influence impact decreases with increasing of Γ_r. When Γ_r is sufficiently high angles, the separation distance of the forward and rear wings far enough, the effect completely disappears and the pressure distribution of the rear wing does not change significantly. When the rear wing dihedral angle increases, the height of vertical tail and endplates are increased. Therefore, the structural weight of the whole machine also increases. In addition, remaining other parameters unchanged, the shortening of chord lengths will lead to a reduction in the absolute wing thickness, which affect the installation of the embedded antenna and the height of the antenna array, and cause a decrease of detection range. When Γ_r is increased from 10° to 25°, the forward-looking and backward-looking detection ranges decrease by about 2.9km and 2.5km, respectively.

2) ENDPLATE HEIGHT RATIO

As shown in Fig. 22, when the endplate height ratio, z_d/z_0 is lower than 0.2, the changes of the lift-to-drag ratio are complex. This complexity results from the interference of the vortex generated by the endplate with the rear wing. When z_d/z_0 is greater than 0.2, the lift-to-drag ratio increases only slightly. Moreover, the endplate height ratio does not affect the radar detection distance but does increase the structural weight. These are because the increase of z_d/z_0 only increase the height of vertical tail and endplates without changing overhead plane parameters.

Fig. 23 shows that as the vortex generated at the endplate trailing edge flows from the lower surface of the rear wingtip, trailing edge separation occurs. Trailing edge separation reduces the aerodynamic efficiency of the rear wing. When z_d/z_0 is increased, the distance between the forward and rear wings also increases, which reduces the interference between the forward and rear wings. Therefore, when z_d/z_0 increases to 0.2, the flow field at the rear wing section near the endplate is dominated by the attached flow regime.

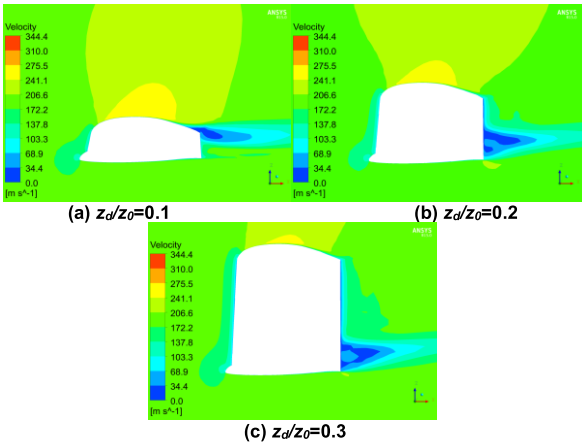

FIGURE 23. Velocity contours of endplate position at different endplate height ratio.

3) JOINT LOCATION

As observed in Fig. 24, the aerodynamic characteristics perform extremely poorly when the joint location is moved outward. The lift-to-drag ratio increases as the forward wing aspect ratio, A_f, is increased, but this influence weakens as the joint location moves outward. Outward movement of joint location causes an increase of both the rear wing aspect ratio and the distance between the forward and rear wings. As well, this results in a decrease in the span of the forward wing. These changes result in the noticeable increase of structural weight, which is similar to the conclusion in [6]. Moreover, the outward movement of joint location increases the rear wing aspect ratio, which reduce the absolute thickness of the wings. Considering the antenna embedded inside the wing, the height of the antenna array is reduced, which causes a significant decrease in the embedded radar detection range. When $A_f = 20$, and b_r/b_f is increased from 0.6 to 0.9, the forward-looking and backward-looking detection ranges decrease by about 12.8km and 12.2km, respectively.

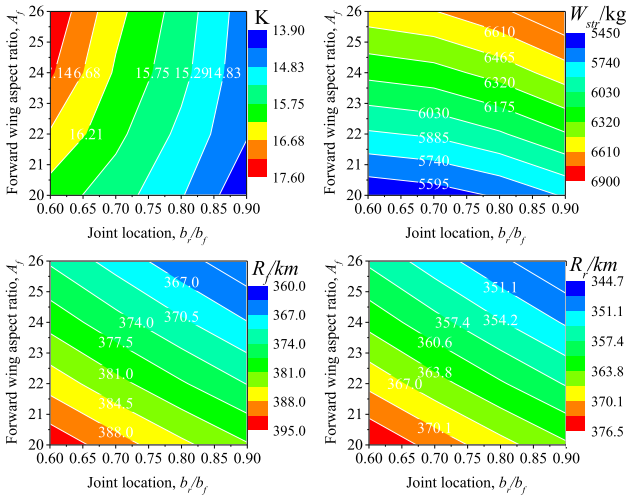

FIGURE 24. Aerodynamic characteristics, structural weights, and detection ranges vary with joint location.

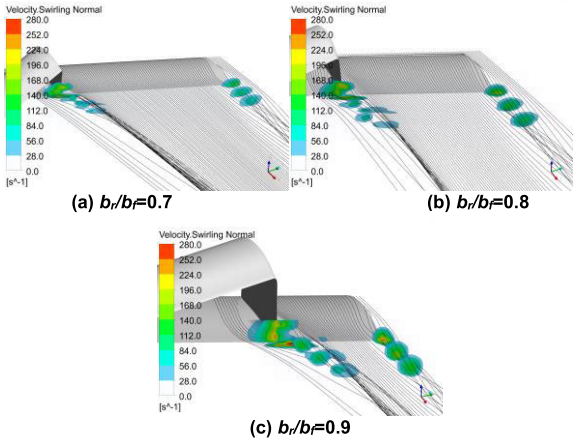

FIGURE 25. Vortex contours and streamlines at different joint locations.

As shown in Fig. 25, the vortices generated by the endplate cause the airflow on the front wing outside the endplate to flow outward in the spanwise direction. When the joint location is moved outside, the interference between this endplate vortex and the wingtip vortex cause a drag increase. In addition, the forward-swept rear wing can transport the boundary layer of the forward wing outside the endplate to the wing-root section. This is beneficial to reduce tendency for flow separation on the forward wing outside the endplate. However, as the endplate moves outward, the area of the forward wing section outside the endplate becomes smaller. As a result, this change in endplate location reduces the positive influence and causes an increase in drag.

V. CONCLUSION

In this work, a suitable joined-wing configuration structural weight estimation model and an embedded radar performance estimation model were established. Subsequently, an integrated multi-objective optimization which coupled aerodynamics, structure, and radar performance was performed.

Results of the aircraft optimization demonstrates the importance of integrating aerodynamics, structure, and radar performance when assessing the design performance of the joined-wing SensorCraft. Compared with the baseline design, the lift-to-drag ratio of the multi-objective compromise result is 14.76% higher than the baseline design. Moreover, the structural weight is reduced by 6.0%, and the forward-looking and backward-looking radar detection ranges increase by 3.96% and 8.75%, respectively.

The sensitive analysis displays that the shape parameters of the joined-wing configuration have a greater impact on the aerodynamic, structure and embedded radar performance and the coupling between different disciplines is obvious. Selection of airfoil, the forward wing aspect ratio, joint location, and the chord length ratio has significant impact on radar detection range.

Using the optimization model established in this paper, aerodynamic, structural, and radar performance can be comprehensively considered. Therefore, a more balanced design can be achieved. This work therefore provides a reference for the future optimization and design of joined-wing SensorCraft.

REFERENCES

[1] J. Martinez, P. Flick, J. Perdzock, G. Dale, and M. Davis, "An overview of SensorCraft capabilities and key enabling technologies," in *Proc. 26th AIAA Appl. Aerodyn. Conf.*, Aug. 2008, pp. 1–13.
[2] D. Lucia, "The SensorCraft configurations: A non-linear aeroservoelastic challenge for aviation," in *Proc. 46th AIAA/ASME/ASCE/AHS/ASC Struct., Struct. Dyn. Mater. Conf.*, Apr. 2005, pp. 1–7.
[3] J. Wolkovitch, "Joined wing aircraft," U.S. Patent 3 942 747, Mar. 9, 1976.
[4] J. Wolkovitch, "The joined wing—An overview," *J. Aircr.*, vol. 23, no. 3, pp. 161–178, Mar. 1986.
[5] M. F. Samuels, "Structural weight comparison of a joined wing and a conventional wing," *J. Aircr.*, vol. 19, no. 6, pp. 485–491, Jun. 1982.
[6] H. Miura, A. T. Shyu, and J. Wolkovitch, "Parametric weight evaluation of joined wings by structural optimization," *J. Aircr.*, vol. 25, no. 12, pp. 1142–1149, Dec. 1988.
[7] S. Smith, S. Cliff, and I. Kroo, "The design of a joined wing flight demonstrator aircraft," Stanford Univ., CA, USA, Tech. Rep. AIAA PAPER 87-2930, Sep. 1987.
[8] B. Oligney, M. Frash, and T. Yechout, "Aerodynamic evaluation and optimization of the Houck joined wing aircraft," in *Proc. 46th AIAA Aerosp. Sci. Meeting Exhib.*, Jan. 2008, pp. 1–11.
[9] J. Pérez-Álvarez, C. Cuerno-Rejado, and J. Meseguer, "Aerodynamic parametric analysis of an unconventional joined-wing aircraft configuration," *Proc. Inst. Mech. Eng., G, J. Aerosp. Eng.*, vol. 230, no. 10, pp. 1917–1933, Aug. 2016.
[10] E. Livne, "Aeroelasticity of joined-wing airplane configurations–past work and future challenges–a survey," in *Proc. 19th AIAA Appl. Aerodyn. Conf.*, Jun. 2001, pp. 16–19.
[11] J. Schwartz, R. Canfield, and M. Blair, "Aero-structural coupling and sensitivity of a joined-wing SensorCraft," in *Proc. 44th AIAA/ASME/ASCE/AHS/ASC Struct., Struct. Dyn., Mater. Conf.*, Apr. 2003, p. 1580.
[12] R. Cavallaro and L. Demasi, "Challenges, ideas, and innovations of joined-wing configurations: A concept from the past, an opportunity for the future," *Prog. Aerosp. Sci.*, vol. 87, pp. 1–93, Nov. 2016.
[13] S. A. Andrews and R. E. Perez, "Comparison of box-wing and conventional aircraft mission performance using multidisciplinary analysis and optimization," *Aerosp. Sci. Technol.*, vol. 79, pp. 336–351, Aug. 2018.
[14] G. W. Reich, D. E. Raveh, and P. S. Zink, "Application of active-aeroelastic-wing technology to a joined-wing SensorCraft," *J. Aircr.*, vol. 41, no. 3, pp. 594–602, May 2004.

[15] B. Smallwood, R. Canfield, and A. Terzuoli, "Structurally integrated antennas on a joined-wing aircraft," in *Proc. 44th AIAA/ASME/ASCE/AHS/ASC Struct., Struct. Dyn., Mater. Conf.*, Apr. 2003, p. 1459.
[16] M. Ceze, M. Hayashi, and E. Volpe, "A study of the CST parameterization characteristics," in *Proc. 27th AIAA Appl. Aerodyn. Conf.*, Jun. 2009, p. 3767.
[17] G. Becker, M. Schäfer, and A. Jameson, "An advanced NURBS fitting procedure for post-processing of grid-based shape optimizations," in *Proc. 49th AIAA Aerosp. Sci. Meeting Including New Horizons Forum Aerosp. Expo.*, Jan. 2011, p. 891.
[18] D. Ma, Y. Zhao, Y. Qiao, and G. Li, "Effects of relative thickness on aerodynamic characteristics of airfoil at a low Reynolds number," *Chin. J. Aeronaut.*, vol. 28, no. 4, pp. 1003–1015, Aug. 2015.
[19] R. Langtry and F. Menter, "Transition modeling for general CFD applications in aeronautics," in *Proc. 43rd AIAA Aerosp. Sci. Meeting Exhib.*, Jan. 2005, pp. 1–14.
[20] R. M. Hicks and S. E. Cliff, "An evaluation of three two-dimensional computational fluid dynamics codes including low Reynolds numbers and transonic mach numbers," NASA, Washington, DC, USA, Tech. Rep. TM-102840, 1991.
[21] D. Ma, G. Li, M. Yang, and S. Wang, "Research of the suction flow control on wings at low Reynolds numbers," *Proc. Inst. Mech. Eng., G, J. Aerosp. Eng.*, vol. 232, no. 8, pp. 1515–1528, Jun. 2018.
[22] E. Torenbeek, *Development and Application of a Comprehensive, Design-Sensitive Weight Prediction Method for Wing Structures of Transport Category Aircraft*, document LR 693, TU Delft, 1992.
[23] K. A. Norton and A. C. Omberg, "The maximum range of a radar set," *Proc. IRE*, vol. 35, no. 1, pp. 4–24, Jan. 1947.
[24] J. Marcum, "A statistical theory of target detection by pulsed radar," *IEEE Trans. Inf. Theory*, vol. 6, no. 2, pp. 259–267, Apr. 1960.
[25] L. V. Blake, "Recent advancements in basic radar range calculation technique," *IRE Trans. Mil. Electron.*, vol. MIL-5, no. 2, pp. 154–164, Apr. 1961.
[26] J. Clarke, "Airborne early warning radar," *Proc. IEEE*, vol. 73, no. 2, pp. 312–324, Feb. 1985.
[27] P. G. Davies and E. J. Hughes, "Medium PRF set selection using evolutionary algorithms," *IEEE Trans. Aerosp. Electron. Syst.*, vol. 38, no. 3, pp. 933–939, Jul. 2002.
[28] K. Q. Ye, "Orthogonal column Latin hypercubes and their application in computer experiments," *J. Amer. Stat. Assoc.*, vol. 93, no. 444, pp. 1430–1439, Dec. 1998.
[29] J. D. Martin and T. W. Simpson, "Use of kriging models to approximate deterministic computer models," *AIAA J.*, vol. 43, no. 4, pp. 853–863, Apr. 2005.
[30] S. Jeong, M. Murayama, and K. Yamamoto, "Efficient optimization design method using kriging model," *J. Aircr.*, vol. 42, no. 5, p. 1375, 2012.

CHENG HE received the B.S. and M.S. degrees in aircraft design from Beihang University, Beijing, China, in 2018, where he is currently pursuing the Ph.D. degree with the School of Aeronautic Science and Engineering. His current research interests include aircraft design and aerodynamic design, especially aircraft design.

YUHONG JIA received the M.S. degree in mechanics and the Ph.D. degree in aircraft design from Beihang University, Beijing, China, in 1993 and 1999, respectively. She is currently a Professor with Beihang University, Beijing. Her current research interests include aircraft design and aircraft structure design.

DONGLI MA received the B.S. and M.S. degrees in flight mechanics and the Ph.D. degree in aircraft design from Beihang University, Beijing, China, in 1990 and 1996, respectively. Since 2001, he has been a Professor with Beihang University, Beijing. His main research interests include aircraft design and UAV technology.

GANG CHEN received the B.S. degree in aircraft design from Beihang University, Beijing, China, in 2015, where he is currently pursuing the Ph.D. degree with the School of Aeronautic Science and Engineering. His current research interests include aircraft design and aerodynamic design.